Dynamics of phase separation in two-dimensional fluids: Spinodal decomposition

S. W. Koch,* Rashmi C. Desai,† and Farid F. Abraham
IBM Research Laboratory, San Jose, California 95193
(Received 6 August 1982; revised manuscript received 29 November 1982)

An extensive computer simulation investigation of the time dependence of spinodal decomposition in a two-dimensional, one-component fluid is reported. This investigation includes constant-temperature and constant-energy simulations, both of which are followed to very long times. We observe the detailed density morphology, finding different growth regions for the average size of the formed liquid clusters. The late-time growth law for the average cluster size is found to be $t^{1/2}$ for the isothermal and $t^{1/3}$ for the constant-energy simulation, respectively. The physical origin of these results is explained by asymptotic analysis of the governing equations of cluster growth. A linear hydrodynamic theory for the early stages of the separation process is also presented.

I. INTRODUCTION

The phenomenon of phase separation is a common occurrence in nature. In technological applications one often needs to mix or unmix various substances (metals, glasses, polymers, and various other chemical species). It is therefore of great importance to study in detail the properties and behavior of a variety of systems undergoing phase separation. The systems of technological importance are often complex, whereas basic understanding is easier to obtain from simpler systems. Because of the importance of this subject area there is a vast amount of literature.[1–6]

Our purpose here is to present an in-depth computer simulation study of the dynamics of phase separation for a two-dimensional unstable fluid. In contrast to laboratory experiments, there is relatively little work in the dynamics of fluid phase separation using numerical simulation experiments, the exception being Abraham *et al.*[1] We use a molecular-dynamics simulation method to study the time evolution of a system which is initially quenched to the unstable region of its thermodynamic phase diagram. This is the relevant quench for the phenomenon of spinodal decomposition. Our numerical experiments are described in detail in Sec. II. [Even though we have done some study of quenches into the metastable region (nucleation) we choose not to present it here.] The results of the numerical experiments on spinodal decomposition are described in Sec. III. These include (i) the configuration snapshots, (ii) cluster distribution, (iii) time-dependent radial distribution function, and (iv) the structure factor, as they evolve in time. Laboratory experiments[4] on spinodal decomposition have probed only the structure factor, and, in this respect, numerical experiments certainly provide much greater detail and finer description of the physical phenomena. Laboratory experiments and numerical simulations are also complimentary to one another in regards to the time scales probed. In general, laboratory diffraction experiments cannot probe very short times and are therefore performed often in the critical region of binary fluid mixtures, where characteristic time scales are much longer compared to the conceptually simpler, one-component fluid system which is separating into liquid and vapor phases. As can be seen from the results in Sec. III, the characteristic time scale for the significant phase separation in a two-dimensional, argon-like, Lennard-Jones fluid is approximately several hundred picoseconds; near its triple point by far the most interesting features of the dynamic phenomena already occur by 300 ps. For a one-component system quenched to realizable distances very close to the critical point, the time duration of the phase separation is very short for a meaningful x-ray diffraction experiment. Thus, none so far have been reported to our knowledge. In Sec. IV we give the theoretical analysis of the experimental results of Sec. III. Our discussion of the characteristic time scales given below in this section becomes more meaningful from the linear stability analysis described in Sec. IV C.

Since we present here numerical experiments on a one-component, two-dimensional system, two further remarks can be made: (i) Much of the theoretical analysis for binary mixtures as well as for one-component systems (presented in Sec. IV) is independent of dimensionality. Advantage of the present two-dimensional study is that the time evo-

lution of the density fluctuation can be visually seen directly from the configuration snapshots. (A movie for quench A discussed in Sec. III has also been made.) With the advent of accurate experimental and theoretical studies of monolayer rare-gas films on graphite substrate (to which the film couples only weakly), the present study is also quantitatively relevant. (ii) Since, in the area of spinodal decomposition, most laboratory experiments have been done on binary mixtures and numerical experiments presented here are for a one-component system, it is also important to appreciate an essential difference in the physics of these two systems. (For a detailed discussion on this point, see Ref. 7.) For the fluid-fluid phase separation in the binary fluid mixture the relevant fluctuations are in the local concentration variable which, in a first approximation (at the level of Cahn-Cook theory), decouples with the other hydrodynamic variables—there is only one conservation law. The fluid-fluid phase separation is an instability driven via a negative thermodynamic derivative of chemical potential with respect to concentration and one introduces a negative diffusion coefficient phenomenologically. For the liquid-vapor phase separation in a one-component system, on the other hand, there are two conservation laws: (a) Local fluid density, leading to the continuity equation of hydrodynamics which couples to the other conserved variable, the local momentum density; (b) for the momentum density one may either write the equation of motion at the level of Euler's equations or the Navier-Stokes equation. Both contain the reversible pressure gradient term which has the negative (isothermal) compressibility, responsible for driving the liquid and vapor phases to separate. The essential change in the fluid hydrodynamic modes (as compared to the single-phase regions of the thermodynamic phase diagram) is that (provided the quench is within the spinodal) during the dynamic evolution of the phase-separation process, $C_p < C_v$ (instability) and the sound speed c_0 becomes purely imaginary (negative compressibility); none of the hydrodynamic modes are propagating (C_p and C_v are heat capacities at constant pressure and constant volume, respectively). The characteristic time scale τ is determined from the unstable mode (one of the acoustic modes) in which the negative compressibility enters: $\tau = ic_0 k$ where k is a typical wave number for the unstable modes. For our numerical experiments this is of the order of a picosecond, and the maximum times to which the experiments were done are 460 ps for the constant-temperature run (quench A) and 300 ps for the constant-energy run (quench C).

The theoretical analysis sketched in Sec. IV also includes the asymptotic analysis of cluster growth in a one-component system (Sec. IV B). This is similar to that done by Lifshitz and Slyozov for binary mixtures. The asymptotic time dependency of the mean cluster radius is found to be $t^{1/2}$ for the isothermal time evolution and $t^{1/3}$ for the adiabatic condition. The experimental results for quench A and C, respectively (Sec. III), support this theoretical finding. In Sec. IV A, we also present a calculation of the coarse-grained radial distribution function and its scaling properties using a simple model. The results show good qualitative agreement with the experimental radial distribution functions. The model contains the essential ingredients of the dynamical evolution and can be improved to obtain better quantitative agreement. The linear stability analysis used in Sec. IV C is similar to our earlier work for a three-dimensional one-component system.[7]

II. MOLECULAR-DYNAMICS SIMULATION EXPERIMENT

A. Numerical method

In the molecular-dynamics method one solves numerically Newton's equations of motion for a given number of particles in a cell, which interact by a specified interaction potential. Since this method is described in various references,[8] we do not discuss it in great detail. As a result of the simulations, one obtains the positions and the velocities of all particles as a function of time. Because the number of coupled differential equations which can be solved simultaneously on a computer is restricted by the available computer time and storage space, one has to deal with a relatively small number of interacting atoms. These are typically several hundred up to a few thousand. However, if one wants to simulate a quasi-infinite system, one applies periodic boundary conditions. This means, that the computational cell is surrounded by identical cells with the same atomic configuration. Each particle has its periodic images, all of which behave identically. If a particle leaves the computational cell at one side, one of its periodic images enters the cell from the opposite site, so that the number of particles in the cell is fixed.

Because one deals with a closed system in a molecular-dynamics experiment, the total energy is constant (within the numerical accuracy). However, a constant-temperature experiment can also be performed, simulating the physical properties of the coupling of the system to a heat bath by simply rescaling the velocities of all atoms at every time interval τ_T, so that the mean kinetic energy corresponds to the desired temperature T.[9]

B. Simulated system

In our experiments we deal with a two-dimensional system of 5041 atoms which interact by the Lennard-Jones potential

$$\phi(r)=4\epsilon\left[\left[\frac{\sigma}{r}\right]^{12}-\left[\frac{\sigma}{r}\right]^{6}\right],$$

where r is the interatomic separation and ϵ,σ are the Lennard-Jones parameters. This potential is known[10] to be a fairly good representation of the interatomic potential for the rare-gas atoms. Thus, with appropriate parameters ϵ,σ our system is a model of a physisorbed monolayer of, e.g., argon on a structureless substrate (e.g., graphite). Since we want to investigate the time dependence of phase-separation processes in this system and are interested in the long-time behavior, we need a fast integration routine with high numerical accuracy. Therefore, we use the fifth-degree Nordsiek-Geer algorithm described in Ref. 11 and a very small integration time step of 0.01 ps. The physical parameters which we have to specify for our experiments are the temperature and the area; i.e., the density since we are always dealing with a fixed number of atoms.

Information regarding these parameters is obtained from the phase diagram of a two-dimensional Lennard-Jones system, which was recently calculated and verified using Monte Carlo techniques by Barker, Henderson, and Abraham.[12] A cut through this phase diagram in the temperature-density plane is shown in Fig. 1. The solid lines are the phase boundaries and the dashed line is the spinodal which was calculated using two-dimensional liquid-state perturbation theory.[13]

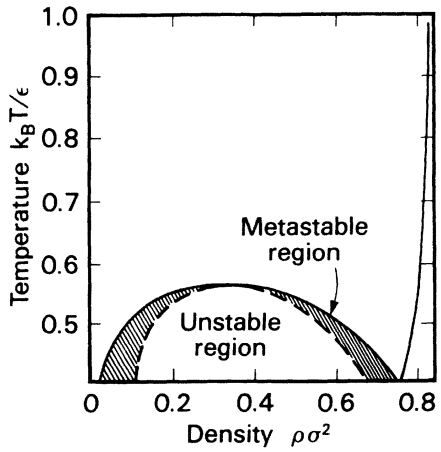

FIG. 1. Phase diagram of the two-dimensional Lennard-Jones system in the density-temperature plane. Dashed curve indicates the spinodal separating unstable and metastable regions.

Generally, our experiments on phase separation are done by quenching the system from various initial configurations, in which we have a one-phase situation, into the unstable region of the phase diagram. These quenches are done by quasi-instantaneous changes in the temperature and/or the density of the system. A quench into the unstable region allows us to study phase separation by the mechanism of spinodal decomposition.[1,14] This is the instability of a homogeneous fluid to infinitesimal fluctuations, which are sufficiently large in extent, that the surface free-energy contribution is always smaller than the volume free-energy contribution. Thus, one expects to observe with increasing time a decomposition process in which highly interconnected regions appear with densities slightly above and slightly below the mean density. These regions will break up into regions with high and low densities, which eventually approach the equilibrium liquid and gas density, respectively. Spinodal decomposition has to be distinguished from nucleation, which occurs if one quenches into the metastable region of the phase diagram. Generally, nucleation[1] is the instability of the homogeneous fluid to density fluctuation with a large amplitude and short wavelength, i.e., the creation of critical droplets of liquid density. These droplets grow until the equilibrium situation of liquid-gas coexistence is reached. (See Fig. 2 for a pictorial description of the two types of density fluctuations and the corresponding phase instability phenomena.)

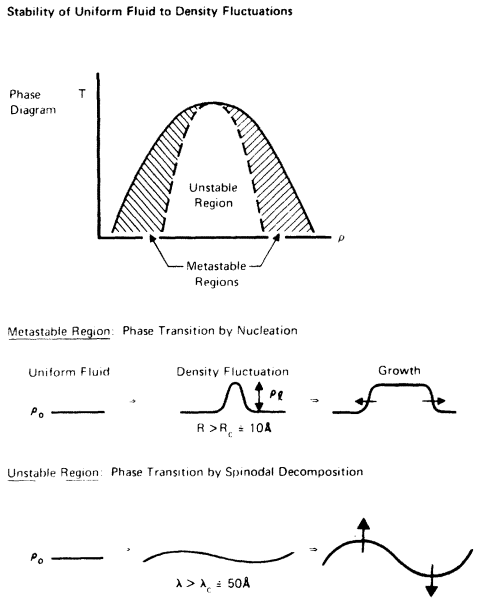

FIG. 2. Pictorial representation of the type of density fluctuations that lead to nucleation in the metastable region and spinodal decomposition in the unstable region.

C. Quenches to the unstable region of the fluid phase diagram

We have performed several experiments (A–C) in order to observe spinodal decomposition under various experimental conditions. The experiments to be discussed are as follows.

(A) The fluid is initiated by placing the atoms in a triangular lattice of density $\rho\sigma^2=0.325$ with a Boltzmann velocity distribution corresponding to a temperature $k_BT/\epsilon=0.45$.[15] Thus, the density is the critical density for liquid-vapor coexistence and the temperature is slightly above the triple-point temperature.[12] At each time step the atomic velocity distribution is renormalized in order to fix the average temperature to $k_BT/\epsilon=0.45$. This initialization guarantees that we start with a uniform distribution of atoms in a very unstable part of the two-dimensional fluid phase diagram.

(B) The system is equilibrated at a temperature $k_BT/\epsilon=1.0$ and a density $\rho\sigma^2=0.8$, i.e., in the one-phase region of the phase diagram. Then a quasi-instantaneous quench is performed to the same point as in experiment A, i.e., the velocities are rescaled to the temperature $k_BT/\epsilon=0.45$ and the distances are rescaled to the density $\rho\sigma^2=0.325$, respectively. The comparison between experiments A and B allows us to study the influence of the prequench state on the experimental results after the quench.

(C) The system is equilibrated at a temperature $k_BT/\epsilon=0.65$ and a density $\rho\sigma^2=0.325$. Then it is quenched to the point $k_BT/\epsilon=0.42$, $\rho\sigma^2=0.325$. The velocities are rescaled to the temperature $k_BT/\epsilon=0.42$ for 2000 time steps (20 ps). From then on, no velocity rescaling was done, i.e., the total energy was fixed. This constant-energy experiment allows us to study the latent-heat effects in spinodal decomposition.

As a result of the molecular-dynamics experiments, one obtains the position of all atoms as a function of time. Using this information, one can calculate various physically interesting quantities, such as the time-dependent radial distribution function $g(r,t)$

$$g(r,t) \propto \langle \delta\rho(\vec{r},t)\delta\rho(0,t) \rangle \ .$$

By Fourier transformation one obtains the time-dependent structure factor

$$S(k,t) \propto \int d\vec{r}\, g(r,t) e^{i\vec{k}\cdot\vec{r}} \ .$$

These quantities can be compared to theoretical results.

Furthermore, one can directly visualize the dynamics of the simulated process by plotting the atomic configuration for various times. This creates "snapshot pictures" and gives information on the time evolution of the atomic density distribution. From the atomic configurations one can also obtain the cluster size distribution at various times.[16] In order to do this, one introduces a critical distance R_c such that all pairs of atoms with pair distance below R_c are counted within the same cluster. We will now discuss our experimental results in detail.

III. EXPERIMENTAL RESULTS

A. Experiment A

Starting from a triangular lattice of density $\rho\sigma^2=0.325$ and $k_BT/\epsilon=0.45$ we performed a constant-temperature simulation.[15] We ran this simulation for a very long time to 45 000 time steps, i.e., 450 ps, because we were also interested in the late-time behavior and especially in scaling of $g(r,t)$ or $S(k,t)$, respectively. The physical meaning of "very long" is discussed in Sec. IV C.

Figure 3 shows a temporal sequence of atomic configurations starting at 5 ps after the quench up to one of the final configurations at 450 ps. Up to 20 ps, one clearly sees the wavelike decomposition

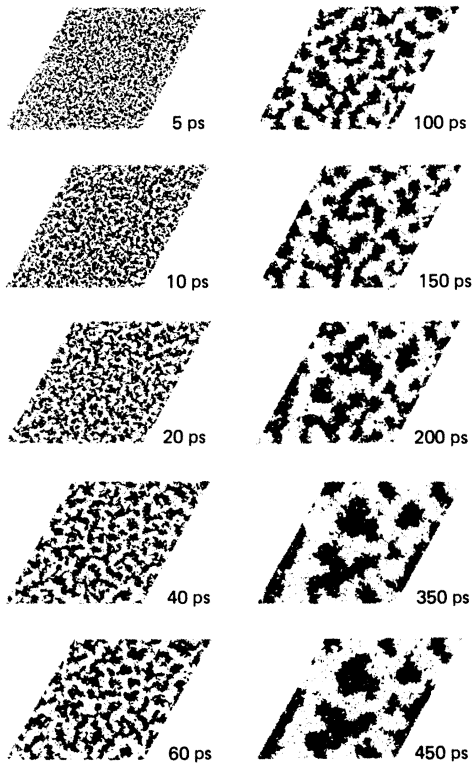

FIG. 3. Snapshot pictures of the constant-temperature simulation ($k_BT/\epsilon=0.45$, $\rho\sigma^2=0.325$) for various times shown in picoseconds after the initialization (experiment A, see text).

process yielding highly interconnected regions of high and low densities, respectively. Around 40 ps, this regime, which may be characterized "wave creation and growth," changes into a regime, which may be characterized as "wave necking" or breakup, leading to the creation and subsequent growth of atomic clusters. These atomic clusters grow until only very few large clusters exist. From the cluster distribution study, we find that the largest of these clusters has ~ 2500 atoms around 400 ps from the total of 5041 atoms in the system.

Figure 4 shows the radial distribution function $g(r,t)$ for the same times at which Fig. 3 shows the atomic configuration. The radial distribution function is numerically calculated by counting the number of atom pairs at distances between r and $r+\Delta r$. The cutoff at large r is determined by the size of the computational cell. Because we are dealing with a large system of 5041 particles, we have on the order of 12 500 000 pairs in our system. Therefore, we can choose a very small Δr in order to obtain the detailed structures in the radial distribution function. [We choose Δr such that we evaluate $g(r)$ in 1000 "bins," i.e., $r_{\max}/\Delta r = 1000$.] We note the short-range liquid-state atomic order which is represented in $g(r)$ by the pronounced small period oscillations for a radial distance of 5σ, this order becoming time invariant around approximately 40 ps. In addition,

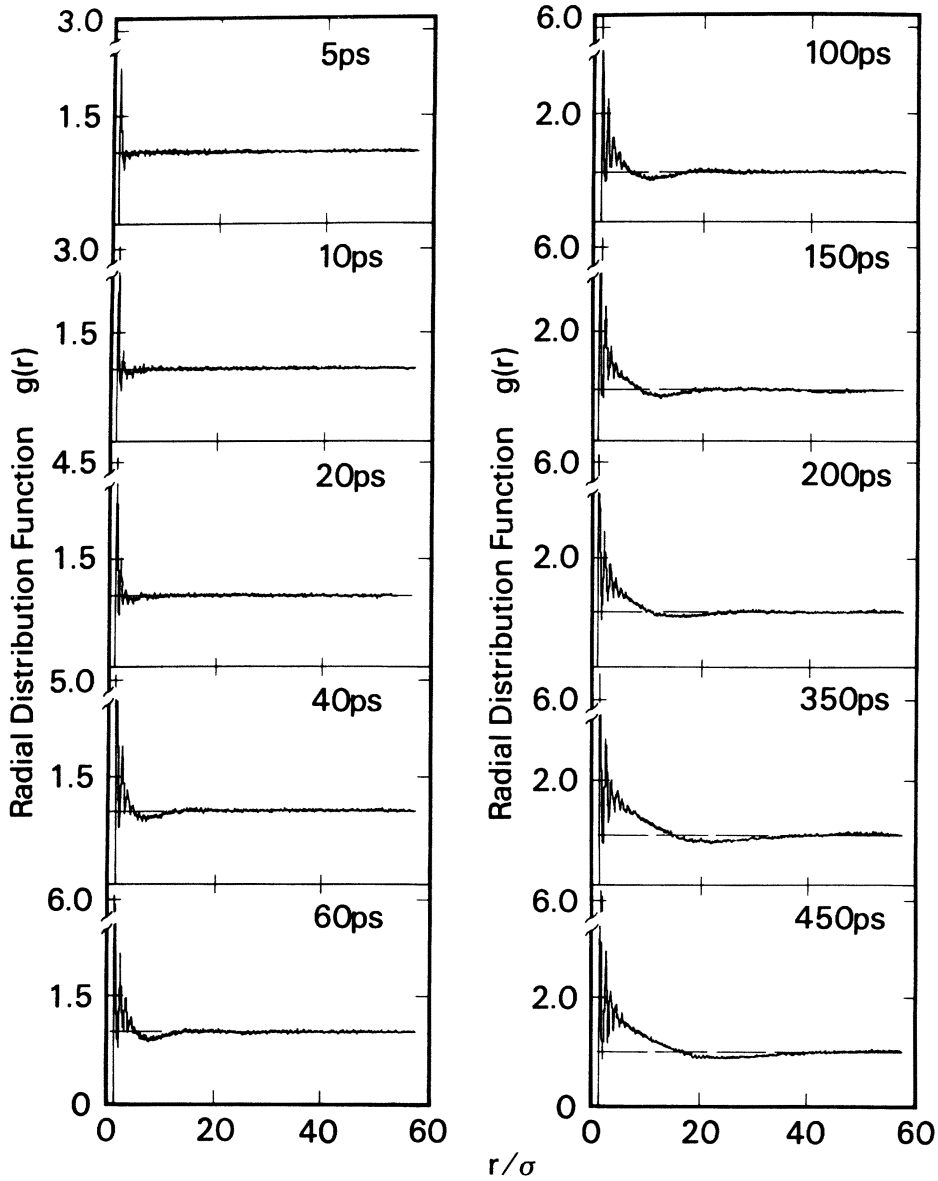

FIG. 4. A sequence of radial distribution functions calculated from the configurations shown in Fig. 3.

a damped oscillation with growing amplitude and period is evident for all times, representing a growing long-range order with a spatial scale that is time dependent. This is simply a consequence of the continuous partitioning of atoms to condensed regions which grow in size.

In terms of the Fourier transform of the radial distribution function, the structure factor $S(k,t)$, the short-range liquid peak appears at a wave number $k\sigma=5.87$, as shown in Fig. 5. The liquid peak saturates in amplitude after 30 ps. Figure 5 shows that a small k peak already appears at $k\sigma=1.33$ by 4 ps and continues to grow. This is the peak corresponding to the spinodal phase-separation process.

As we can see from Fig. 6, this growth in amplitude continues to the longest times in our simulation. Simultaneously, we observe a shift of the small-k-peak position to decreasing wave numbers with increasing time, indicating the coarsening process in the density pattern (compare Fig. 3).

In order to analyze the scaling behavior connected with the phase-separation process, we calculate a coarse-grain radial distribution function by averaging over radial intervals greater than the period characteristic of the atomic short-range order and arbitrarily take as a measure of the coarse-grain "average size" of the growing liquid regions the radial distance at which this distribution function first equals unity. In Fig. 7, this average cluster size $R(t)$ is presented as a function of time on a double-logarithmic plot and exhibits a $t^{0.20}$ dependence during the early stage of the phase-separation process

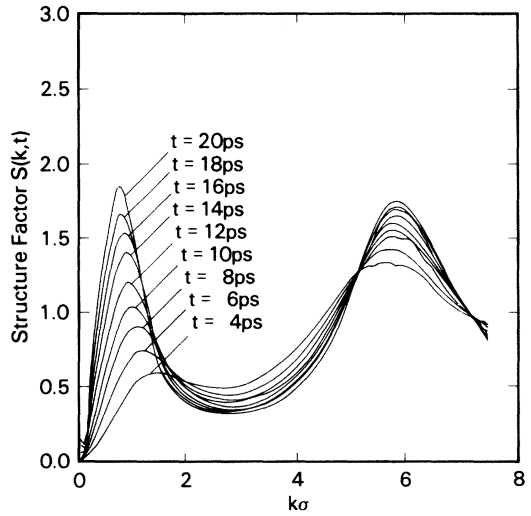

FIG. 5. Experimental structure factor $S(k,t)$ vs k for various early times after the initialization of the simulated system at $k_BT/\epsilon=0.45$, $\rho\sigma^2=0.325$ (experiment A, see text).

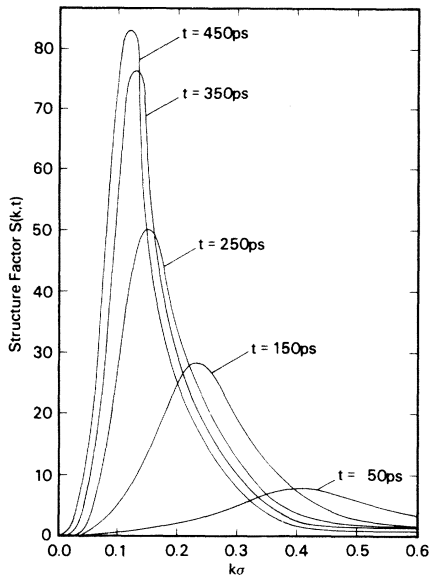

FIG. 6. Long-time behavior of the spinodal peak of the structure factor $S(k;t)$; compare Fig. 5. Note especially the magnitudes in vertical scales in Fig. 5 and in this figure.

$(0<t\lesssim 30$ ps), followed by a change to a one-half power dependence for the remainder of the simulation ($50<t<450$ ps). A careful examination of the time developing interatomic morphologies for these different growth stages suggests that they may be characterized as wave creation and growth until local maxima in density approach the condensed liquid density, followed by wave necking or breakup leading to the creation and subsequent growth of macroscopic clusters. One may correctly state that the "spinodal mechanism" comes to completion by

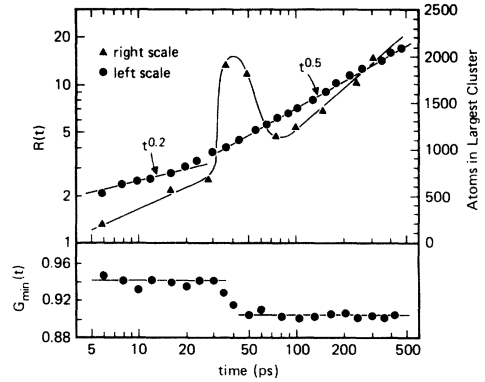

FIG. 7. Cluster size $R(t)$ (●, upper left scale), minimum of radial distribution function $G_{\min}(r,t)$ (●, lower left scale), and the size of the longest cluster (▲, upper right scale) as a function of time (experiment A, see text).

about 30 ps since the density extremes have been achieved. After this early time, coarsening dynamics by vapor condensation and/or cluster coagulation are the governing mechanisms.

The two stage growth of clusters is also substantiated by examining two further characteristics. (i) The magnitude of the minimum of $g(r)$ versus time is shown in the lower part of Fig. 7. It clearly shows the two growth stages. (ii) From the atomic configurations (Fig. 3), we have also studied directly the cluster size distribution using the algorithm outlined in Ref. 16. In Fig. 7 (upper right scale, ▲), we show the size of the largest cluster as a function of time. This demonstrates the phenomenon of wave creation up to about 30 ps, manifesting itself as the appearance of a very large growing cluster due to the highly interconnected morphology. Subsequently, there is a wave-necking transition region around 40–50 ps. This is followed by "isolated" cluster growth (compare Fig. 3).

A simple scaling of coarse-grain radial distribution functions with time is suggested if we hypothesize that the density morphology remains approximately topologically invariant during coarsening, but the actual spatial variation of density domains expands as $R(t)$. We conclude that within the framework of this picture, a time-invariant radial distribution function $G(X)$ is obtained from the relation

$$G(X)=g(X,t),\quad X=r/R(t)\ , \tag{1}$$

where $g(r,t)$ is the measured coarse-grain distribution function at time t. In Fig. 8, the scaled function $G(X)$ is presented for various times and for the two different growth regimes. We see very good scaling invariance for the two growth regimes, with the invariance at later times breaking down for $X>2.0$. This failure only reflects the fact that the average nearest-neighbor separation distance does not scale with average cluster size $R(t)$ when the system coarsens to a few large clusters, a consequence of the conservation of the total number of atoms. In actual fact, the scaled coarse-grain distribution function $G(X)$ for distances $X<2.0$ reflects principally the structure of an individual "average" cluster of normalized size $X=1.0$, the cluster's structure described by the peculiarities of radially averaging over atom positions in the cluster. We conclude that $G(X)$ is a rather insensitive measure of the system's density morphology and that it is not very astonishing that we find a scaling invariance for relation (1). This scaling behavior $G(X)$ is reflected in a scaling invariance for the growing peak in the structure factor $S(k)$; i.e.,

$$S(K)-1=[S(k,t)-1]/[R(t)]^2\ ,$$

$$K=R(t)k\ . \tag{2}$$

In Sec. IV B of this paper we present a theoretical explanation of the $t^{0.5}$ power-law behavior of $R(t)$.

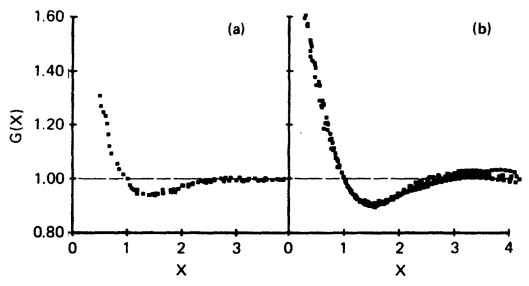

FIG. 8. Scaled radial distribution function $G(X)$, $X=r/R(t)$, for the two-time regimes in experiment A: (a) 12, 14, 16, 18, 20, 22, 24, 26 ps and (b) 40, 60, 80, 100, 200, 300, 400, 450 ps.

B. Experiment B

In this experiment we equilibrated the system at a temperature $k_BT/\epsilon=1.0$ and a density $\rho\sigma^2=0.8$. Figure 1 shows that this is in the one-phase region of the phase diagram. After equilibrium is reached, we quenched the system to the same point as in experiment A, i.e., to $k_BT/\epsilon=0.45$, $\rho\sigma^2=0.325$. This quench was done "quasi-instantaneously," i.e., we rescaled all velocities, so that the mean kinetic energy corresponds to the temperature $k_BT/\epsilon=0.45$, and rescaled all distances, so that the density $\rho\sigma^2$ be-

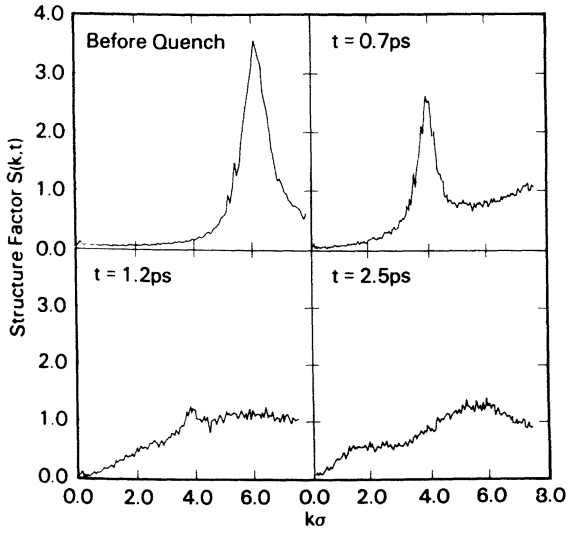

FIG. 9. Experimental structure factor for the quench from $\rho\sigma^2=0.8$, $k_BT/\epsilon=1$ to $\rho\sigma^2=0.325$, $k_BT/\epsilon=0.45$ (experiment B) for very early times after the quench showing the loss of the memory of the prequench condition.

comes 0.325. This experiment was done in order to investigate if and how the prequench state of the system influences the results after the quench.

In Fig. 9 we show, as an illustrative example, the structure factor $S(k,t)$ of our system at different times. We see that $S(k,t)$ in the prequench situation has the typical shape of an equilibrium liquid with one peak around $k\sigma=6.2$. Immediately after the quench, we see this peak shifting to lower k values (due to the rescaling, i.e., expansion of the distances in our system) and the peak amplitude decreasing, while at the same time a "background" starts to build up. By about 2.5 ps the memory of the prequench situation at high temperature and density is lost.

As a comparison, we have plotted in Fig. 10 the structure factor for very early times for experiment A. At 1 ps we see a lot of spikes, the memory of the triangular lattice, the structure of which is a δ function at $k\sigma=3.85$. These spikes vanish very rapidly and by about 3—4 ps after the quench the memory of the triangular lattice is lost. If we call this time at which the memory is lost $t=0$, then at subsequent times experiments A and B show the same behavior and yield the same (time-averaged) quantities. Thus, we conclude that our experiments are, after a short initialization period, rather insensitive to the prequench conditions.

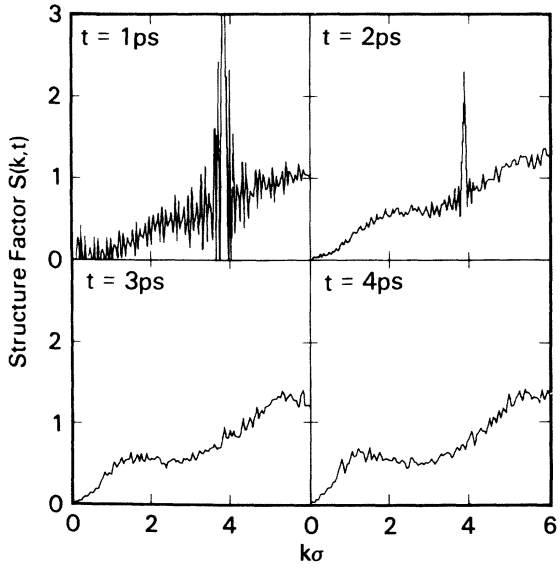

FIG. 10. Experimental structure factor for experiment A (see text) for very early times after the initialization, showing the loss of the memory of the initialization in a triangular lattice.

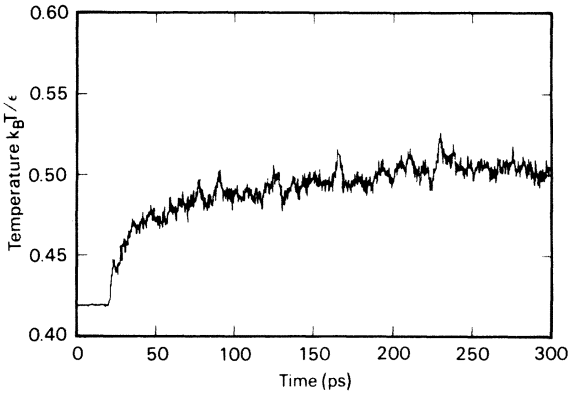

FIG. 11. Time evolution of the system temperature k_BT/ϵ (averaged over 10 time steps) vs time for the constant-energy simulation (experiment C; see text).

C. Experiment C

In this experiment we equilibrated our system at $k_BT/\epsilon=0.65$ and $\rho\sigma^2=0.325$, i.e., in the one-phase region of the phase diagram but relatively close to the phase boundary. Then we quenched it quasi-instantaneously to $k_BT/\epsilon=0.42$, keeping the density fixed. At this point we ran it for 2000 time steps, i.e., 20 ps, as a constant-temperature simulation. After that, we no longer rescaled the velocities, i.e., we performed a constant-energy experiment. Figure 11 shows how the temperature of the system behaves as a function of time. Approximately 60 ps after we stopped the velocity rescaling, k_BT/ϵ approaches a value at 0.5, and fluctuates around 0.5—0.505 during the remainder of the simulation. This temperature value is still well below the critical temperature as can be seen from Fig. 1.

However, if we had not fixed the temperature to $k_BT/\epsilon=0.42$ for 20 ps, the system temperature would have increased very rapidly and exceeded T_c so that the system would have gone again into the single-phase region of the phase diagram. We analyzed this experiment in the same way as experi-

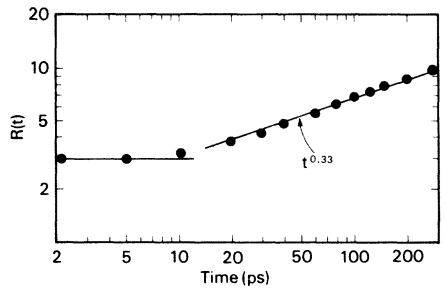

FIG. 12. Cluster size $R(t)$ as a function of time for the constant-energy simulation (experiment C; see text).

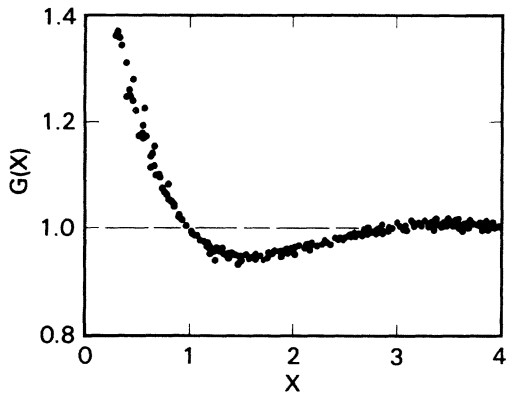

FIG. 13. Scaled radial distribution function $G(X)$, $X=r/R(t)$ for the $t^{0.33}$ scaling regime in experiment C (see text) at 30, 50, 80, 120, 160, 210, 240, 270, 300 ps.

ment A. A comparison shows that the time evolution is much slower than in experiment A. In order to express this quantitatively, we plot in Fig. 12 the average cluster size $R(t)$ obtained from the coarse grain $g(r)$ in the same way as described earlier. Figure 12 shows that $R(t)$ is only very weakly time dependent for very early times up to 10 ps, followed to a one-third power dependence for the remainder of the simulation, i.e., up to 300 ps. This growth law of $t^{1/3}$ for constant-energy simulation compared to $t^{1/2}$ for constant-temperature simulation is understood theoretically and discussed in Sec. IV B of this paper. Figure 13 shows the scaled $G(X)$ obtained using Eq. (1). Again, we see very good scaling invariance during the times from 30 to 300 ps.

IV. THEORETICAL ANALYSIS

A. Model calculation for the pair correlation function

In Sec. III we showed that experimental coarse-grain radial distribution function $g(r,t)$ obeys very good scaling invariance. The scaling was suggested through the hypothesis that during the coarsening process the density morphology remains topologically invariant while the actual spatial variation of density domains expands as the typical cluster size grows. In this section we discuss a very simple model of the inhomogeneous density distribution for the phase-separating system which contains the essential ingredients of the dynamical evolution. For the model we evaluate the radial distribution function $g(r,t)$, then show that it obeys scaling, and compare the scaled distribution $g(X)$ with the experimental results shown in Fig. 8.

The model system consists of a "mother-cluster" of size $R_1(t)$, surrounded by a shell of vapor concentric with the mother cluster and of outer radius $R_2(t)$, which in turn is surrounded by a uniform fluid of mean density with which the system began its time evolution (and which "macroscopically" is always constant). For simplicity we assume that the density variation in the model system is such that (i) within the mother cluster the density is ρ_l, the final equilibrium density, (ii) the density in the vapor shell is zero, and (iii) the density is ρ_m, the uniform mean density in the outermost region. The conservation of the total number of atoms in the system implies that $R_2=(\rho_l/\rho_m)^{1/2}R_1$. The model is schematically shown in Fig. 14. The center of the mother cluster is at O. In order to obtain the coarse-grain distribution function $g(r,t)$ we need to average over the point Q around which a circular shell of radius r to $r+dr$ would be drawn to count the number of atoms in this shell, i.e.,

$$g(r)=\langle g(r,X_0)\rangle_{X_0} = \frac{1}{\pi R_1^2}\int_0^{R_1} g(r,X_0)2\pi X_0 dX_0 \ . \tag{3}$$

The time dependence arises entirely from that of R_1. In Fig. 14, for a typical X_0, a circle of radius r is shown as the dashed circle $P_1P_2P_3P_4P_5$. It is obvious that the integrand in Eq. (3) is given by

$$g(r,X_0)=\frac{1}{2\pi r\rho_m}\left[\rho_l\int_{P_1}^{P_2} ds+\rho_m\int_{P_3}^{P_5} ds\right], \tag{4}$$

where the integration is along the dashed circle. The geometrical problem is quite straightforward to solve once it is treated as a superposition of two simpler problems in which the density distributions, as seen from the center of the mother cluster, are

$$\rho_1(R)=\begin{cases}\rho_l, & 0<R<R_1\\ 0, & R>R_1\end{cases} \tag{5a}$$

and

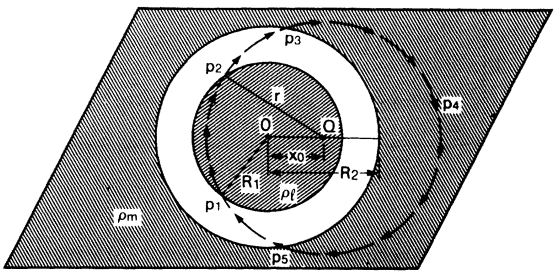

FIG. 14. Model for the theoretical calculation of the coarse-grain radial distribution function (see text).

$$\rho_2(R)=\begin{cases}0, & 0<R<R_2\\ \rho_m, & R>R_2\end{cases} \tag{5b}$$

respectively. The result is

$$g(r)=g_1(r)+g_2(r)\ , \tag{6a}$$

where $g_1(r)$ and $g_2(r)$ involve the following integral:

$$I(a,b,\eta,\alpha)=\int_a^b \arccos\left[\frac{|\eta^2+x^2-\alpha|}{2\eta x}\right]x\,dx \tag{6b}$$

and are given by

$$g_1(r)=\begin{cases}\delta^2\left[Y^2+\frac{2}{\pi}[I(Y,1,X,1)-I(1-X,Y,X,1)]\right], & \text{if } 0<X<1\\ \frac{2}{\pi}\delta^2 I(X-1,1,X,1)\ , & \text{if } 1<X<2\\ 0\ , & \text{if } X>2\end{cases} \tag{6c}$$

and

$$g_2(r)=\begin{cases}0\ , & \text{if } 0<X<(\delta-1)\\ \frac{2}{\pi}I(\delta-X,1,X,\delta^2)\ , & \text{if } (\delta-1)<X<(\delta^2-1)^{1/2}\\ 1-Z^2+\frac{2}{\pi}[I(\delta-X,Z,X,\delta^2)-I(Z,1,X,\delta^2)]\ , & \text{if } (\delta^2-1)^{1/2}<X<\delta\\ 1-\frac{2}{\pi}I(X-\delta,1,X,\delta^2)\ , & \text{if } \delta<X<(\delta+1)\\ 1\ , & \text{if } X>(\delta+1)\end{cases} \tag{6d}$$

where $X=r/R_1$, $Y=(1-X^2)^{1/2}$, $\delta^2=\rho_l/\rho_m$, and $Z=(\delta^2-X^2)^{1/2}$. The result, as expected, depends only on two variables: $r/R_1(t)$ and ρ_l/ρ_m. Thus, for the model, the scaling as defined in Eq. (1) is satisfied when ρ_l and ρ_m are fixed given values. If one performs a series of experiments with varying quench depth, then the superposition of scaled $G(X)$ of the type shown in Fig. 8 will not hold. In the model there are actually two length scales R_1 and R_2. The number conservation relates these two:

$$R_2=\left[\frac{\rho_l}{\rho_m}\right]^{1/2}R_1$$

and the interrelation involves the quench depth.

Numerical integration of Eq. (6a) for $\rho_l=0.71$, $\rho_m=0.325$ (conditions for the simulations discussed in Sec. III) shows that as r increases, $g(r)$ becomes unity at $r\approx 1.25R_1$. Thus, in order to compare the model result to the experimental distribution shown in Fig. 8, we use $R(t)=1.25R_1(t)$. This comparison is shown in Fig. 15. It is clear that the simple model contains all the essential ingredients to understand the experimental scaling. The quantitative differences between the model and experiment arise from our assumptions of (i) sharp interfaces at R_1 and R_2, (ii) approximating the vapor region by vacuum, and (iii) approximating the second shell of clusters by the mean density fluid which starts sharply at R_2.

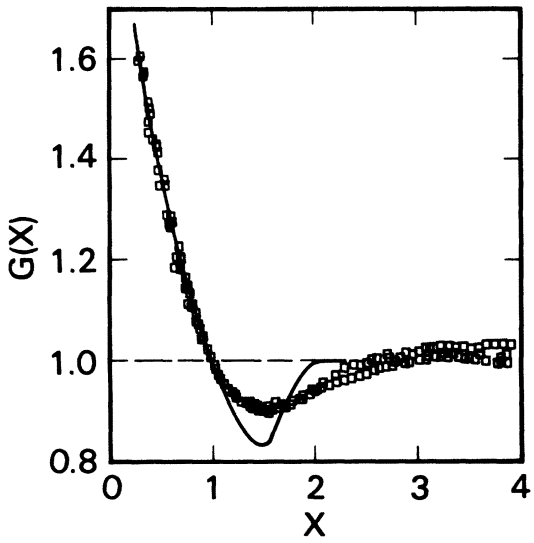

FIG. 15. Comparison between model-radial distribution function (full line) and experimental results (squares), taken from Fig. 8(b).

B. Asymptotic analysis for cluster growth

From the constant-temperature simulation experiment A, we showed in Fig. 7 that for large times the mean cluster radius grows as $t^{1/2}$. In contrast, for a constant-energy simulation we find (Fig. 12) that asymptotically the growth law is consistent with $t^{1/3}$ with the exponent 0.33 ± 0.05. In this section we give an asymptotic analysis for these simulation results.

The classic work relevant to our analysis is that of Lifshitz and Slyozov.[17] They study the cluster growth for a binary mixture and conclude that the radius of the cluster $R(t)$ would grow as $t^{1/3}$ for large times. This result can be shown to be independent of dimensionality and would hold in both two- and three-dimensional systems. Their basic starting equation for $R(t)$ is

$$\frac{dR}{dt}=\frac{D}{R}\left[\Delta-\frac{\alpha}{R}\right], \tag{7}$$

where D is the diffusion coefficient of particles across the cluster boundary, Δ is the degree of supersaturation, and α is a parameter related to surface tension. By supplementing this equation with the matter conservation law and the equation of continuity for the cluster distribution function, Lifshitz and Slyozov not only show that $R(t)\sim t^{1/3}$ asymptotically but also explicitly evaluate the asymptotic cluster size distribution. Recently, Turski and Langer[18] have studied the dynamics of a diffuse liquid-vapor interface for a one-component system. Even though they applied hydrodynamics only to evaluate early time nucleation rate and did not investigate asymptotic cluster growth, they obtain an equation [their Eq. (4.15)] for $R(t)$ which is identical in form to Eq. (7) above. In this analysis the combination $(D\Delta)$ of Eq. (7) is replaced by

$$(2\lambda\sigma T)/l^2 n_l R^*) ,$$

where λ is thermal conductivity, σ surface tension, l the latent heat, n_l the liquid density at temperature T, and R^* the critical droplet radius. It is quite simple to start with such an equation for $R(t)$ and extend Lifshitz-Slyozov analysis to one-component systems to arrive at $t^{1/3}$ growth law for adiabatic (constant-energy) simulation regardless of dimensionality.

For our isothermal simulation of the one-component, two-dimensional Lennard-Jones system, we now briefly describe how a Lifshitz-Slyozov-type asymptotic analysis leads to a growth law where $R(t)\sim t^{1/2}$. Our starting point is the rate equation for the number of particles n in the cluster

$$\frac{dn}{dt}=g_n-l_n . \tag{8a}$$

The right-hand side of this equation, the particle current at the cluster boundary is the difference between a gain term due to the monomers impinging from the low-density vapor at temperature T and a loss term from the cluster due to evaporation at the surface. We have made a movie of the atomic trajectories in our isothermal simulation. From this, we find that the motion of atoms in the vapor phase is kinematic (nondiffusive). Thus, we use the kinetic theory to write the gain term as

$$g_n=n_v(t)S(T/2\pi m)^{1/2} , \tag{8b}$$

where $S=2\pi R$ is the surface of the two-dimensional cluster and $n_v(t)$ is the vapor density at time t. In terms of n_v and the equilibrium liquid density n_l the supersaturation $\Delta(t)=n_v(t)/n_l$ and the number of particles in the cluster n is related to the cluster radius as $n=\pi R^2 n_l$ if we assume that at late stages the density within the cluster is n_l. Then Eq. (8a) becomes

$$2\pi R\frac{dR}{dt}=\Delta(t)2\pi R\left[\frac{T}{2\pi m}\right]^{1/2}-\frac{l_n}{n_l} . \tag{8c}$$

For the loss term, we can use the classical nucleation theory, where the competition between the surface and volume energy terms enables the droplet to grow or shrink. The total loss rate from the cluster surface S can then be written as

$$l_n=AS\,e^{-\phi/T}e^{\alpha/R} , \tag{8d}$$

where A is a proportionality constant, ϕ the volume energy, and α/R the surface contribution. In a similar context (but for a different system) these ideas have been used to analyze the finite lifetime effects in electron-hole droplet formation.[19] There the loss term would arise due to thermionic emission-type result given by the so-called Richardson-Dushman equation in which ϕ would be the electronic work function and the constant A would be given by $(4\pi m T^2)/h^3$. In the asymptotic analysis, the explicit expression for A is irrelevant; it is only the form of the equation for $R(t)$ that matters. One gets

$$\frac{dR}{dt}=\Delta(t)\left[\frac{T}{2\pi m}\right]^{1/2}-\left[\frac{A\,e^{-\phi/T}}{n_l}\right]e^{\alpha/R} . \tag{9a}$$

For large time α/R is rather small and it is appropriate to write $e^{\alpha/R}=1+\alpha/R$ which leads to

$$\frac{dR}{dt}=\left[\frac{\alpha}{R_c(t)}-\frac{\alpha}{R}\right]b , \tag{9b}$$

where a critical droplet radius $R_c(t)$ can be defined from Eq. (9a) by setting $dR/dt=0$. The remaining proportionality constant b provides for the scaling of time t. It is convenient to render Eq. (9b) dimensionless by introducing the following quantities: R_{c0}, the initial value of the critical radius which would depend on the initial supersaturation Δ_0, a scaling time $T=R_{c0}^2/b\alpha$ and dimensionless supersaturation $x(t)=R_c(t)/R_{c0}$; the variables R and t are changed to $\rho=R/R_{c0}$ and $t'=t/T$. Then we get

$$\frac{d\rho}{dt'}=\frac{1}{\rho}\left[\frac{\rho}{x(t')}-1\right], \tag{10}$$

which is one of the starting equations for the asymptotic analysis. To a good approximation, the quantity $x(t')$ is $\Delta_0/\Delta(t)$ and becomes large at large times since $\Delta(t)$ approaches zero. Once Eq. (10) is established the remaining details of our asymptotic analysis are trivial extensions of the work of Lifshitz and Slyozov to two dimensions. This is described elsewhere.[20] The area distribution of clusters is obtained from such an analysis. When expressed in terms of reduced variables $z=\rho^2/x^2(t')$ and $\tau=\ln[x^2(t')]$, the distribution is

$$\phi(z,\tau)=\begin{cases} n(\tau)p(z,\gamma_0), & z\le z_0=4 \\ 0, & z\ge z_0 \end{cases} \tag{11}$$

where the number of clusters per unit area is

$$n_0(\tau)\equiv\int_0^\infty \phi(z,\tau)dz=A\,e^{-\tau}, \tag{12}$$

$$p^*(\sqrt{z},\gamma_0)=\begin{cases} \dfrac{\sqrt{z}\exp\left[-\sqrt{z}\Big/\left[1-\dfrac{\sqrt{z}}{2}\right]\right]}{2-\left[1-\dfrac{\sqrt{z}}{2}\right]^4}, & \sqrt{z}\le 2 \\ 0, & \sqrt{z}\ge 2\,. \end{cases} \tag{17}$$

This is shown in Fig. 16. In the analysis[20] we also find that

$$\langle(z^{1/2}-1)\rangle\equiv\int_0^{z_0}p(z,\gamma_0)(z^{1/2}-1)dz=0\,, \tag{18}$$

i.e.,

$$\langle z^{1/2}\rangle=\left\langle\left[\frac{\rho}{x(t')}\right]\right\rangle=1\,. \tag{19}$$

We also obtain the asymptotic growth law as

$$\langle\rho\rangle=x(t')=\frac{1}{\sqrt{2}}(t')^{1/2} \tag{20}$$

in conformity with the results of numerical simulation shown in Fig. 7. The cluster size distribution in Eq. (17) cannot be verified from our molecular-dynamics simulation experiment since the actual number of droplets in late states of the simulation is quite small.

and the probability that a cluster will have reduced area between z and $z+dz$ is

$$p(z,\gamma_0)=\begin{cases} e^{-\psi}/v_R(z,\gamma_0), & z\le z_0=4 \\ 0, & z\ge z_0\,. \end{cases} \tag{13}$$

Here

$$v_R(z,\gamma_0=4)=-(2-z^{1/2})^2\,, \tag{14}$$

$$\psi(z,\gamma_0=4)=\int_0^z\frac{dz'}{(2-z'^{1/2})^2}=2\ln\left[1-\frac{\sqrt{z}}{2}\right]+\frac{2\sqrt{z}}{2-\sqrt{z}}\,, \tag{15}$$

and

$$A=-\frac{1}{\kappa\int_0^4\frac{e^{-\psi}}{v_R}z\,dz}=\frac{1}{8\kappa[\frac{1}{2}-e^2\mathrm{E}_1(2)]}\,,$$

$$\simeq 0.287\frac{Q_0}{R_{c0}^2}\,, \tag{16}$$

where $\kappa=\pi R_{c0}^2/Q_0$ and Q_0 is the *total* initial supersaturation. Since z is reduced area, it is of interest to find the cluster size distribution

$$p^*(\sqrt{z},\gamma_0)=p(z,\gamma_0)\frac{dz}{dz^{1/2}}\,.$$

It is

C. Linear stability analysis

In this section we use a linear stability analysis for a two-dimensional fluid in the unstable region of the

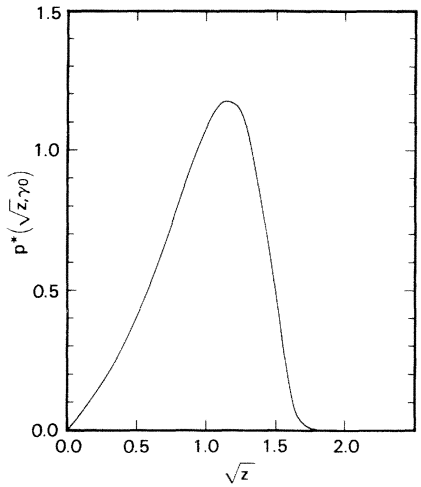

FIG. 16. Cluster distribution function as calculated from the asymptotic analysis of equations for isothermal nucleation theory.

liquid-vapor phase diagram.[7] The analysis is completely analogous to that in Sec. II of Ref. 7, so we only give the results. Briefly, we use the linear hydrodynamic equations which include the stochastic fluctuations in the stress tensors and the heat flux. The nonlocal driving force arising from density inhomogeneities is specified by the van der Waals prescription[1] and is accounted for through the pressure gradient in the dynamical equations. Comparison of the time-dependent structure factor $S(k,t)$ is made with our molecular-dynamics computer experiments. Detailed expression for $S(k,t)$ is given in Ref. 7.

In order to apply the result of linear hydrodynamics to the specific situation of spinodal decomposition, we have to specify the prescription for the equation of state and various transport coefficients. Liquid-state perturbation theories have been successfully applied to the study of the thermodynamics of a constrained single-phase system within the two-phase coexistence region.[1,12] (Such thermodynamic quantities are denoted by a dagger.) The reference system in these theories is one with hard-sphere interaction. In our dynamical calculation it is therefore appropriate to use similar ingredients.

From the Enskog theory of dense fluids,[21] we have the following expressions for the three transport coefficients:

$$\eta=\eta_0(1+y+0.8729y^2)/Y\ , \tag{21a}$$

$$\zeta=\eta_0(1.246y^2)/Y\ , \tag{21b}$$

$$\kappa=\kappa_0(1+1.5y+0.8718y^2)/Y\ , \tag{21c}$$

where $\eta_0=0.511\sqrt{T}/\pi$ and $\kappa_0=2.058\sqrt{T}/\pi$ are the low-density values of the shear viscosity and thermal conductivity, respectively, $Y=y/(\frac{1}{2}\pi\rho_0\sigma^2)$, and Y is the factor by which the binary-collision frequency is increased in the Enskog theory. This factor is usually determined from the knowledge of the equation of state $p^\dagger(\rho,T)$:

$$y=\frac{1}{\rho_0 k_B T}\left[T\left[\frac{\partial p^\dagger}{\partial T}\right]_\rho\right]-1\ . \tag{22}$$

We use a two-dimensional liquid-state perturbation theory[13] to obtain the equation of state $p^\dagger(\rho,T)$ and hence $(\partial p^\dagger/\partial T)_\rho$ and $(\partial p^\dagger/\partial\rho)_T$. In addition, we need to specify only the nonlocal driving term $\mathscr{L}(k)$ which appears in the linear theory. Traditionally, one would use the square gradient theory which was introduced by van der Waals[22] to discuss the liquid-vapor interface and by Cahn[14] in the study of spinodal decomposition of solid solutions. This would imply

$$\mathscr{L}_{\rm vdW}(k)=Ak^2\ . \tag{23a}$$

In any extension of van der Waals theory, one has to explicitly or implicitly specify the direct correlation function $c(k)$. An approximate prescription of $c(k)$ used by Abraham *et al.*[1] gives the generalized van der Waals theory for $\mathscr{L}(k)$. In two dimensions it reads

$$\mathscr{L}_{\rm gvdW}(k)=2\int_0^\infty[\cos(kx)-1]\Omega_0(x)dx \tag{23b}$$

with

$$\Omega_0(x)=\int_{|x|}^\infty dz\frac{z}{(z^2-x^2)^{1/2}}u(z)g_2^\dagger(z,\rho_0)\ ,$$

where the pair-correlation function $g_2^\dagger$ is calculated for the Lennard-Jones fluid using the two-dimensional liquid-state perturbation theory.[13] We have used in our computations both the prescriptions (23a) and (23b) to see how sensitive the qualitative features of $S(k,t)$ are to the choice of $\mathscr{L}(k)$. The dispersion of hydrodynamic modes $\alpha_i(k)$ can also be found in a manner analogous to that in Ref. 7.

In Fig. 17(a) we display $\alpha_i(k)$ for van der Waals ansatz and in Fig. 17(b) the same for generalized van der Waals prescription for $k_BT/\epsilon=0.45$ and $\rho\sigma^2=0.325$. As expected, both of these agree for small k and the general qualitative features are also identical for all k values. For the range of k values shown we get one real and a pair of complex roots which turn into three real roots for large k (not shown in the figures). The real root [always denoted by $\alpha_1(k)$ in the subsequent discussion and by a solid

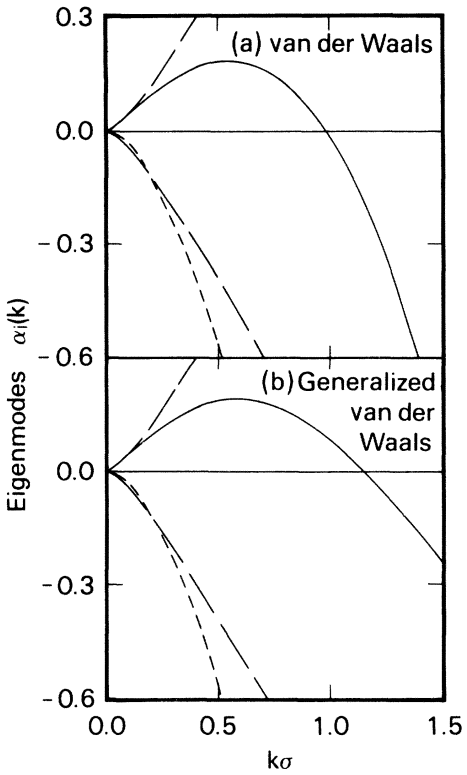

FIG. 17. Dispersion of the hydrodynamic modes within the unstable region of two-dimensional Lennard-Jones liquid-vapor coexistence ($\rho\sigma^2=0.325$, $k_BT/\epsilon=0.45$) using (a) van der Waals theory, and (b) generalized van der Waals theory.

line in Figs. 17(a) and 17(b)] is positive up to some critical wave number k_c and negative thereafter. Thus, for $k<k_c$, we have a growing mode which is related to the hydrodynamic instability in the phase-separation process.

Using the hydrodynamic modes α_i of van der Waals (vdW) and generalized van der Waals (gvdW) theory, we numerically obtain the time-dependent structure factor. The results are plotted in Figs. 18(b) and 18(c) for different times after the quench. For $S(k,0)$ we use the experimental data at $t=4$ ps (since by this time the memory of initial triangular lattice is lost; see Fig. 10 and Sec. III) to be able to compare the theoretically predicted time evolution with experiment. Figures 18(b) and 18(c) show a very similar overall behavior of S_{gvdW} and S_{vdW}. The structure factor in generalized van der Waals theory is broader than S_{vdW} because the critical wave number k_c (gvdW) is larger than k_c (vdW). The faster growth of S(gvdW) reflects the greater positive values of α_1(gvdW) in comparison to α_1(vdW).

In Fig. 18(a) the experimental structure factor (quench A) is replotted for several times after the quench (compare Fig. 5). For small times (lowest curves), theory and experiment agree quite well. For later times, linearized hydrodynamic theory clearly overestimates the absolute $S(k,t)$. Nonlinear contributions will slow down this growth rate.

In order to make a sensitive comparison of our theory with the molecular-dynamics experiment, we deduce an "effective growing mode α_{eff}" from the experimental time-dependent structure factor $S_{\text{exp}}(k,t)$. The manner in which this is done is described in detail in Ref. 7. For our two-dimensional fluid, we follow an identical procedure. In Fig. 19 we present the comparisons for both prescriptions, and for several times after the temperature quench. These times are the earliest measurements in the simulation experiment (after the memory of the prequench situation is lost) where linear behavior is most probable. It is very gratifying that the effective amplification factor α_{eff} is of the same qualitative magnitude as the α_1 for each

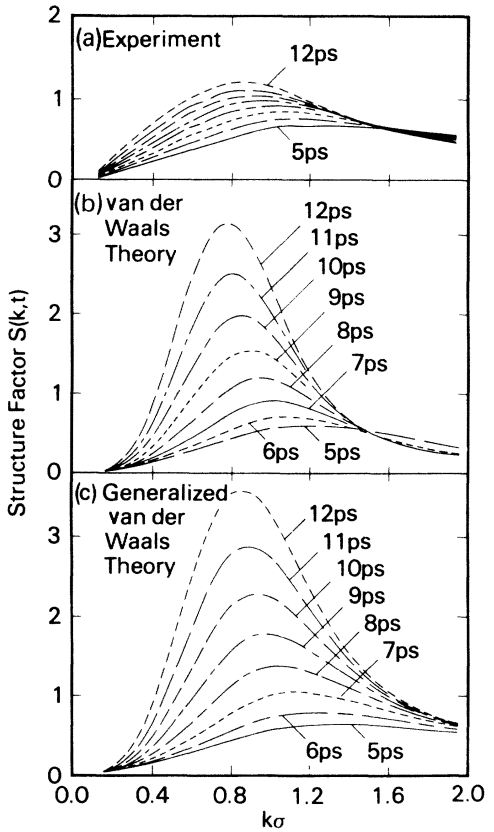

FIG. 18. (a) Experimental structure factor (experiment A) in comparison with theoretical structure factor using (b) van der Waals and (c) generalized van der Waals description.

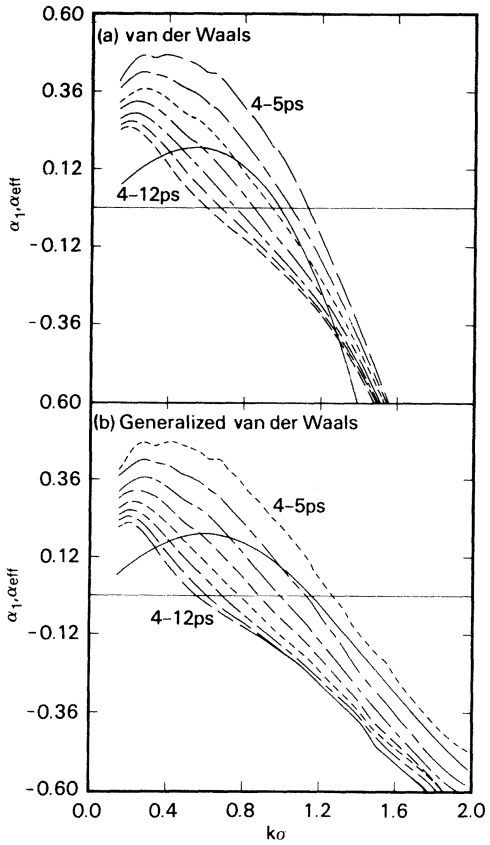

FIG. 19. Comparison of the theoretical growing mode α_1 (solid line) predicted by (a) van der Waals and (b) generalized van der Waals theory with the effective amplification factor α_{eff} (dashed lines) obtained using experimental structure factor measurements for experiment A.

prescription, even though the theory has no adjustable parameters. Quantitatively, both the generalized van der Waals and the van der Waals descriptions yield α_1 and α_{eff} that are in reasonable agreement with experiment. Qualitatively these two-dimensional results are very similar to our three-dimensional results.[7]

V. SUMMARY AND CONCLUSIONS

We have used the technique of molecular-dynamics simulation to study the dynamics of phase separation of a one-component, two-dimensional Lennard-Jones fluid into liquid and vapor phases. A variety of quenches have been made within the coexistence curve of the system and these are described in detail in Sec. II. Specifically, two of the quenches (A and C) have been made to evolve for quite a long time. The isothermal simulation of the quench A to an initially unstable state was run to 460 ps and a similar adiabatic quench C to 300 ps. In contrast to laboratory diffraction experiments these numerical experiments have provided with detailed information about the system trajectories, cluster distribution functions at various times, and the time evolution of the radial distribution function in addition to the structure factor. We have analyzed these results theoretically in Sec. IV. Both $g(r,t)$ and $S(k,t)$ obey scaling relations. A simple model discussed in Sec. IV A describes the observed scaling of $g(r,t)$ quite well. The mean cluster radius is found to grow as $t^{1/2}$ for the isothermal simulation (quench A) and as $t^{1/3}$ for the adiabatic simulation (quench C). These results are explained by our asymptotic analysis for cluster growth given in Sec. IV B. In Sec. IV C we discussed the linear stability analysis for a one-component, initially unstable fluid using equations of fluctuating hydrodynamics. Qualitatively, the structure factor given by the linear theory is found to be of the same order as that found in numerical experiment even though one knows that the nonlinearities are essential in the phenomena of spinodal decomposition. However, the coarsening behavior is found to be in the experimental structure factor even at the earliest of time (approximately 1–2 ps); this is absent in a linear theory and we conclude that there is (quantitatively), strictly speaking, no linear regime in our numerical experiment.

There are important differences, both in detail and in computational concepts of spinodal decomposition in one-component systems like the one studied here and for fluid-fluid phase separation in binary systems for which many experiments exist. These were discussed in detail in the Introduction and also in Ref. 7. There are still many aspects of the experimental results described in Sec. III which require a greater theoretical understanding. At the present time a complete nonlinear theory for spinodal decomposition in a one-component system does not exist even though a useful beginning[7] has been made.

*Present address: Institut für Theoretische Physik, Universität Frankfurt, D-6000 Frankfurt am Main 90, Federal Republic of Germany.

†Permanent address: Department of Physics, University of Toronto, Toronto, Ontario, Canada M5S 1A7.

[1]F. F. Abraham, Phys. Rep. 53, 95 (1979), and references therein.

[2]J. W. Cahn, Trans. Metall. Soc. AIME 242, 166 (1968), and references therein.

[3]J. S. Langer, M. Bar-On, and H. D. Miller, Phys. Rev. A

11, 1417 (1975), and references therein.
[4]W. I. Goldburg, in *Scattering Techniques Applied to Supramolecular and Nonequilibrium Systems,* edited by S. H. Chen, B. Chu, and R. Nossal (Plenum, New York, 1981), pp. 383–409, and references therein.
[5]J. L. Lebowitz, J. Marro, and M. H. Kalos, Acta Metall. 30, 297 (1982), and references therein.
[6]K. Binder, in *Fluctuations, Instabilities and Phase Transitions,* edited by T. Riste (Plenum, New York, 1975), p. 53.
[7]S. W. Koch, R. C. Desai, and F. F. Abraham, Phys. Rev. A 26, 1015 (1982).
[8]See, e.g., J. Kushick and B. J. Berne, in *Statistical Mechanics, Part B: Time-Dependent Processes,* edited by B. J. Berne (Plenum, New York, 1977), Chap. 2; A. Rahman, Phys. Rev. 136, A405 (1964); L. Verlet, *ibid.* 159, 98 (1967).
[9]H. C. Andersen, J. Chem. Phys. 72, 2384 (1980).
[10]J. O. Hirschfelder, C. F. Curtiss, and R. B. Bird, *Molecular Theory of Gases and Liquids* (Wiley, New York, 1964).
[11]A. Nordsiek, Math. Comp. 16, 22 (1962).
[12]J. A. Barker, D. Henderson, and F. F. Abraham, Physica (Utrecht) 106, 226 (1981).
[13]D. Henderson, Mol. Phys. 34, 301 (1977), and references therein.
[14]J. W. Cahn, Acta Metall. 9, 795 (1961).
[15]F. F. Abraham, S. W. Koch, and R. C. Desai, Phys. Rev. Lett. 49, 923 (1982).
[16]S. D. Stoddard, J. Comput. Phys. 27, 291 (1978).
[17]I. M. Lifshitz and V. V. Slyozov, J. Phys. Chem. Solids 19, 35 (1961).
[18]L. A. Turski and J. S. Langer, Phys. Rev. A 22, 2189 (1980).
[19]H. Haug and S. W. Koch, in *Dynamics of Synergetic Systems,* edited by H. Haken (Springer, Berlin, 1980), p. 57.
[20]R. C. Desai, S. W. Koch, and F. F. Abraham, Physica (Utrecht) (in press).
[21]D. M. Gass, J. Chem. Phys. 54, 1898 (1971).
[22]See, e.g., the translation of the 1893 work of van der Waals: J. S. Rowlinson, J. Stat. Phys. 20, 197 (1979).

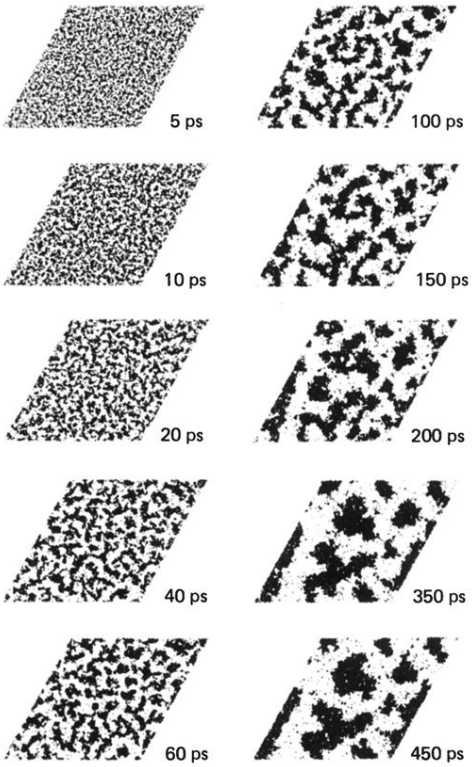

FIG. 3. Snapshot pictures of the constant-temperature simulation ($k_BT/\epsilon=0.45$, $\rho\sigma^2=0.325$) for various times shown in picoseconds after the initialization (experiment A, see text).